Progress In Electromagnetics Research B, Vol. 60, 287–300, 2014

A Recursive Approach to Improve the Image Quality in Well-Logging Environments

Yu-Hsin Kuo and Jean-Fu Kiang*

Abstract—A three-stage recursive approach is proposed to improve the recovered distribution of electric parameters in a well-logging environment. The first stage is executed using the conventional linear sampling method (LSM) and the contrast source inversion (CSI) method. In the second stage, the background distribution is updated to better identify the target shape, using the recovered results in the first stage. In the third stage, the background distribution is made closer to the results in stage two, which improves the recovered distribution near the target boundary. The effect of noise is also simulated.

1. INTRODUCTION

The inverse methods based on scattering waves have been widely applied to estimate the electrical parameters in the medium of interest. The linear sampling method (LSM) has been used to identify the possible target region immersed in the background medium, which helps reducing the follow-up computational time in estimating the electrical parameters [1, 2]. The singular-value decomposition (SVD) technique with Tikhonov regularization and its variant have been applied to solve the equations derived from the LSM [3].

With the target region roughly identified, a contrast source inversion (CSI) method has been applied to estimate the permittivity and conductivity, in both the target region and the background medium. The IE-CSI (integral equation CSI) and the FD-CSI (finite difference CSI) are two typical implementations of the CSI method. The former is suitable for homogeneous or layered background media, and the latter is more suitable for inhomogeneous targets embedded in an inhomogeneous background medium [4–6]. A multiplicative regularized CSI (MR-CSI) method has been claimed to get a sharper image of the target boundary than the other CSI methods [7, 8].

Well-logging (WL) techniques have been widely used for oil exploration [9, 10]. In [11], a formula is derived to estimate the maximum separation between two boreholes, based on the operating frequency, as well as the permittivity and conductivity of the background medium. The operating frequency from 1 kHz to 20 MHz have been adopted [11, 12]. Take sedimentary rocks for example, $\sigma \simeq 1\,\mathrm{mS/m}$ and $\epsilon_r = 9.8$ at 5 MHz, the maximum separation between boreholes is 110 m [11].

In [13], a square tunnel of width 3 m is carved in a background medium with $\epsilon_r = 5$ and $\sigma = 3\,\mathrm{mS/m}$. Two boreholes, separated by 20 m, are drilled for detecting the tunnel. Multiple transmitters and receivers, operating from 2 to 402 MHz, are placed in the boreholes to collect the scattering data. The recovered shape from the permittivity distribution is slightly larger than the real tunnel, but that from the conductivity is slightly smaller. The permittivity and the conductivity around the tunnel boundary are over-estimated. Random ripples appear outside the tunnel and near the tunnel boundary.

In [14], a cylindrical target of radius 0.5 m, with $\epsilon_r = 5$ and $\sigma = 0.1\,\mathrm{mS/m}$, is embedded in a rock background with $\epsilon_r = 4$ and $\sigma = 0.1\,\mathrm{mS/m}$. Two boreholes, separated by 10 m, are used to detect

Received 13 June 2014, Accepted 14 August 2014, Scheduled 26 August 2014

* Corresponding author: Jean-Fu Kiang (jfkiang@ntu.edu.tw).

The authors are with the Department of Electrical Engineering and the Graduate Institute of Communication Engineering, National Taiwan University, Taipei 106, Taiwan.

the target at 160 MHz, with 21 transmitters in the left borehole and 21 receivers in the right borehole, all at a spacing of 0.5 m. Strong random ripples appear in the distributions of permittivity and the conductivity near the target boundary.

In general, strong ripples appear near the boundary of the recovered distributions, leading to a difficult decision on the boundary location. In this paper, a recursive approach, based on the LSM and the CSI method, is proposed to improve the quality of the recovered distributions of permittivity and conductivity in a well-logging environment. The boundary ripples can be reduced. The LSM and the CSI method are briefly reviewed in Section 2, simulation results using the proposed recursive approach are presented in Section 3, and some conclusions are drawn in Section 4.

2. BRIEF REVIEW OF LSM AND CSI METHOD

The linear sampling method (LSM) is used to estimate the shape of the target embedded in the detection domain, D_d, as shown in Fig. 1. The probes are deployed in two parallel boreholes, C_0, outside the detection domain, D_d. After the target shape is estimated, the contrast source inversion (CSI) method is applied to estimate the electric parameters in the target domain, D.

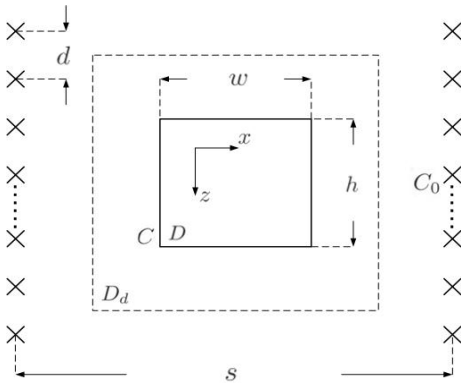

Figure 1. A target in a well-logging environment.

The LSM starts with the scattered field at $\bar{r}$, due to an excitation probe at $\bar{r}\,''$:

$$\bar{E}_s\left(\bar{r},\bar{r}\,''\right) = k_b^2 \iint\limits_{D_d} G\left(\bar{r},\bar{r}\,'\right)\chi\left(\bar{r}\,'\right)\bar{E}_t\left(\bar{r}\,',\bar{r}\,''\right)d\bar{r}\,' \tag{1}$$

where $\bar{E}_s(\bar{r},\bar{r}\,'')$ is the scattered field, $\bar{E}_t(\bar{r}\,',\bar{r}\,'')$ is the total field observed at $\bar{r}\,'$, $\chi(\bar{r}) = [\epsilon(\bar{r}) - \epsilon_b]/\epsilon_b$ is the contrast function of the medium, with $\epsilon(r)$ and ϵ_b being the complex permittivity of the target and the background medium, respectively.

The two-dimensional Green's function, $G(\bar{r},\bar{r}\,')$, satisfies the wave equation

$$\left(\nabla^2 + k_b^2\right)G\left(\bar{r},\bar{r}\,'\right) = -\delta\left(\bar{r}-\bar{r}\,'\right) \tag{2}$$

with the explicit form

$$G\left(\bar{r},\bar{r}\,'\right) = -\frac{j}{4}H_0^{(2)}\left(k_b\left|\bar{r}-\bar{r}\,'\right|\right) \tag{3}$$

where $H_0^{(2)}$ is the zeroth-order Hankel function of the second kind, and k_b is the wavenumber of the background medium.

Define an adjoint field, $\xi(\bar{r})$, which satisfies an adjoint equation

$$\iint\limits_{D_d'} E_s\left(\bar{r},\bar{r}\,''\right)\xi\left(\bar{r}\,',\bar{r}\,''\right)d\bar{r}\,'' = G\left(\bar{r},\bar{r}\,'\right) \tag{4}$$

where all possible excitation probes are located in D_d', which is practically outside of D_d.

If there are M excitation probes, at $\bar{r}_{pn}$'s with $1 \leq n \leq M$, then the integral form in (4) can be discretized into a matrix equation using the LSM. Then apply the singular-value decomposition (SVD) technique and the Tikhonov regularization technique to solve the matrix equation for ξ [1].

Next, define an LSM indicator for a cell centered at $\bar{r}\,'$ as

$$I_{\xi}(\bar{r}\,') = \sum_{n=1}^{M} \zeta_n \left| \xi\left(\bar{r}\,', \bar{r}_{pn}\right) \right|^2 \tag{5}$$

If $I_{\xi}(\bar{r}\,')$ is smaller than a threshold value, $\bar{r}\,'$ is claimed to be within the target domain.

In (4), $G(\bar{r}, \bar{r}\,')$ can be viewed as a scattered field

$$\Psi_s\left(\bar{r}, \bar{r}\,'\right) = -\frac{j}{4} H_0^{(2)}\left(k_b \left|\bar{r} - \bar{r}\,'\right|\right) \tag{6}$$

which is a linear combination of the observed data, $\bar{E}_s$, weighted by $\bar{\xi}$. Similarly, define an incident field, Ψ_i, associated with E_i, as

$$\Psi_i(\bar{r}, \bar{r}\,') = \iint\limits_{D_d'} \xi\left(\bar{r}, \bar{r}\,''\right) E_i\left(\bar{r}\,', \bar{r}\,''\right) d\bar{r}\,'' \tag{7}$$

where $\bar{r}$ indicates an observation point within the target, and $\bar{r}\,'$ indicates a point in the detection domain, D_d. A total field, Ψ_t, can be defined in a similar manner as

$$\Psi_t\left(\bar{r}, \bar{r}\,'\right) = \iint\limits_{D_d'} \xi\left(\bar{r}, \bar{r}\,''\right) E_t\left(\bar{r}\,', \bar{r}\,''\right) d\bar{r}\,'' = \Psi_i\left(\bar{r}, \bar{r}\,'\right) + \Psi_s\left(\bar{r}, \bar{r}\,'\right) \tag{8}$$

where the second identity is derived from $E_t = E_i + E_s$ and the definitions of Ψ_s and Ψ_i in (4) and (7), respectively; The value of $\Psi_t(\bar{r}, \bar{r}\,')$ is obtained by adding (6) and (7).

Next, by substituting (1) into (4), an integral equation of $\chi(\bar{r}\,'')$ is derived as

$$G(\bar{r}, \bar{r}\,') = k_b^2 \iint\limits_{D_d} G(\bar{r}, \bar{r}\,'')\Psi_t(\bar{r}\,', \bar{r}\,'')\chi(\bar{r}\,'')d\bar{r}\,'' \tag{9}$$

which can be transformed into a matrix form to solve for $\chi(\bar{r}\,'')$ in the detection domain, D_d, using the SVD and the Tikhonov regularization technique.

3. RECURSIVE APPROACH AND SIMULATIONS

Figure 2 shows the flowchart of the proposed method, which is consisted of three stages. In the first stage, a contour-like pattern is usually observed in the recovered distribution of permittivity inside the target, while random ripples usually appear outside the target. By guessing different possible target domains based on the contour of permittivity distribution obtained in the first stage, and adopting a linear background profile inside the target, the updated permittivity distribution exhibits a magnitude jump across the boundary of the target domain if the guessed domain is close to the original target domain. Once the target shape is identified more accurately, the third stage is applied by choosing a higher-order polynomial of maximally flat type as the background profile. The updated distributions of permittivity and conductivity is expected to be improved.

Consider a target with rectangular cross section of width $w = 3\,\text{m}$ and height $h = 3\,\text{m}$, as shown in Fig. 1. The target mimics a high-yield oil shale with $\epsilon_r = 4$ and $\sigma = 1\,\text{mS/m}$ [15], embedded in limestone with $\epsilon_r = 6$ and $\sigma = 0.1\,\text{mS/m}$ [16, 17]. The operating frequency is 20 MHz. The two boreholes are separated by $s = 20\,\text{m}$, with 21 probes in each borehole, at a spacing of $d = 1\,\text{m}$. The cell size is $\Delta x = \Delta z = 0.2\,\text{m}$.

Figure 3 shows the recovered distributions of relative permittivity and conductivity after stage 1. It is observed that the equi-ϵ_r contours inside the target are roughly conformal to the shape of the target, while the distribution of ϵ_r outside the target exhibits some random ripples. Next, arbitrarily

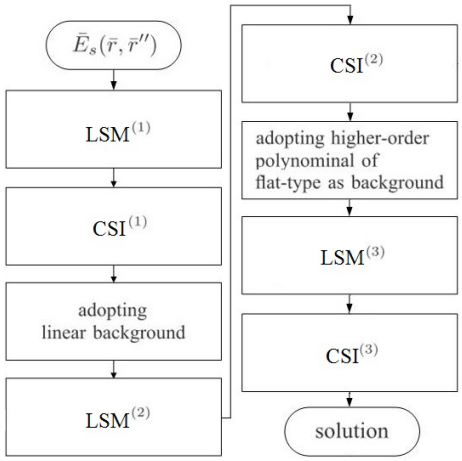

Figure 2. Flowchart of recursive approach.

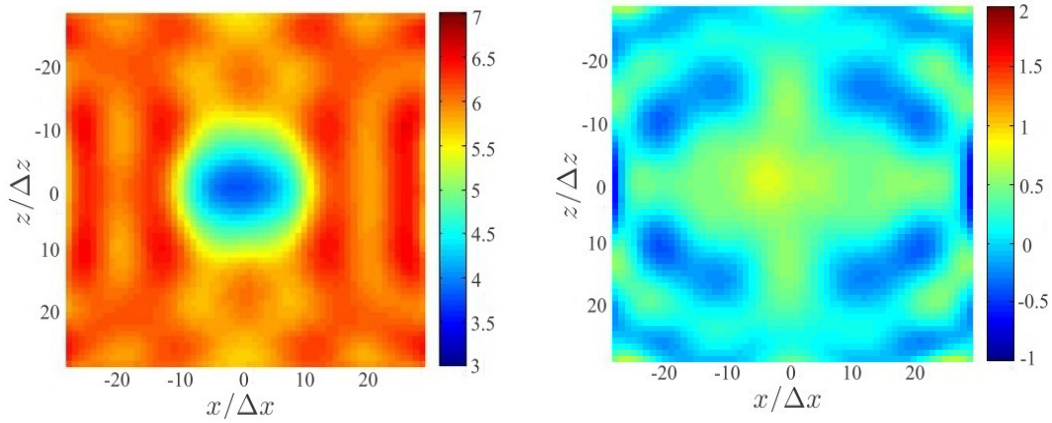

Figure 3. Recovered distributions of (a) relative permittivity and (b) conductivity, after stage 1, with a rectangular target of $\epsilon_r = 4$ and $\sigma = 1\,\mathrm{mS/m}$ embedded in a background of $\epsilon_r = 6$ and $\sigma = 0.1\,\mathrm{mS/m}$.

select three equi-ϵ_r contours, with ϵ_r equal to 4.5, 5 and 5.5, respectively, as a possible target domain, D'.

In stage 2, the background within D' is set as

$$\epsilon_b'(\bar{r}) = \epsilon_{er} + (\epsilon_b - \epsilon_{er}) \left(\frac{|\bar{r} - \bar{r}_c|}{|\bar{r}_e - \bar{r}_c|} \right)^{\alpha} \tag{10}$$

$$\sigma_b'(\bar{r}) = \sigma_{er} + (\sigma_b - \sigma_{er}) \left(\frac{|\bar{r} - \bar{r}_c|}{|\bar{r}_e - \bar{r}_c|} \right)^{\alpha} \tag{11}$$

which is expected to fit more closely with the distributions of the electric parameters within D'; where $\bar{r}_c$ is the geometrical center of D'; ϵ_{er} is the maximum/minimum value of relative permittivity within D'; $\bar{r}_e$ is the intercept point between the contour and a line extended from $\bar{r}_c$ to the point of interest, $\bar{r}$; and σ_{er} is the maximum value of σ within D'.

Figures 4 and 5 show the recovered permittivity and conductivity profiles, respectively, with $\alpha = 1$ and different choices of D'. The guessed target domain, D', bound by the contour of $\epsilon_r = 5$, matches more closely with the original target domain. The corresponding permittivity profile shows a magnitude jump across the boundary of D' and less random ripples outside D'. If the guessed domain, D', is smaller than the original one, the recovered permittivity profile inside D' exhibits a strong random pattern.

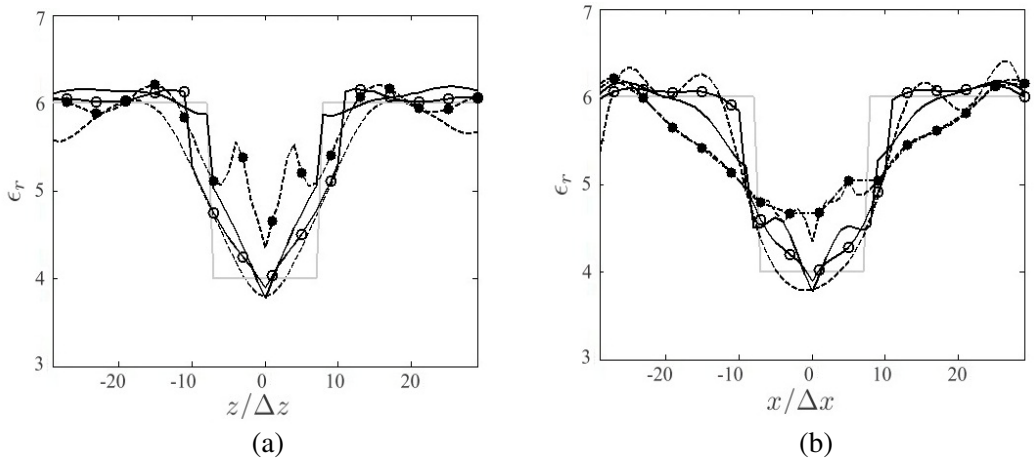

Figure 4. Recovered permittivity profile of the rectangular target described in Fig. 3, (a) at $x = 0$, (b) at $z = 0$; ——— (grey): original, − − −: stage 1, — ∘ — : stage 2 with D' bound by $\epsilon_r \leq 4.5$, ———: stage 2 with D' bound by $\epsilon_r \leq 5$, − − • − −: stage 2 with D' bound by $\epsilon_r \leq 5.5$.

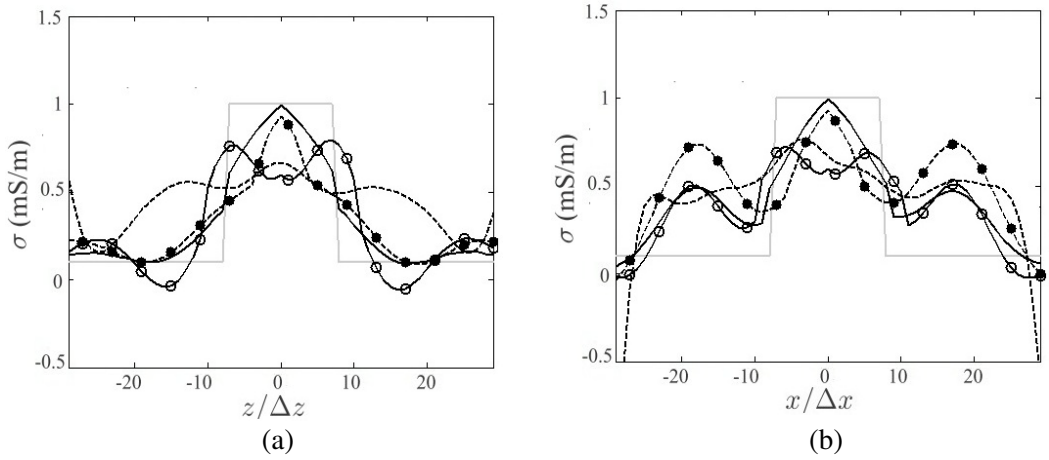

Figure 5. Recovered conductivity profile of the rectangular target described in Fig. 3, (a) at $x = 0$, (b) at $z = 0$; curve legends are the same as in Fig. 4.

With the target shape more accurately identified, stage 3 is applied to better estimate the electric parameters within D'. Eqs. (10) and (11) are used to update the background distributions of ϵ and σ within D'. Different α's are tried to study their effects on the accuracy of the recovered distributions.

Figures 6 and 7 show the recovered permittivity and conductivity profiles, respectively. The permittivity profile around the boundary of target domain shows a stronger magnitude jump than those in stages 1 and 2. The magnitude jumps across the boundary in stage 3, with $\alpha = 2$ and 4, look similar; but the profile inside the target becomes flatter and more uniform with $\alpha = 4$. Fig. 8 shows the final distributions after stage 3, with $\alpha = 4$. Compared with Fig. 3, the conductivity profile is more accurate, and the target boundary appears clearer than that after stage 1.

Next, the permittivity of the target is changed to $\epsilon_r = 8$, to model a low-yield oil shale [15]. The recovered distributions of permittivity and conductivity after stage 1 are shown in Fig. 9. Similar to the high-yield oil shale, the equi-ϵ_r contours inside the target are roughly conformal to the original target shape, and random ripples are observed in the ϵ_r distribution outside the target domain.

Figures 10 and 11 show the recovered permittivity and conductivity profiles, respectively, after stage 2 and stage 3. The contour of $\epsilon_r = 7.1$ is chosen as the boundary of D', based on the results in Fig. 9. In stage 2, the background distributions of ϵ and σ within D' are updated using (10) and (11),

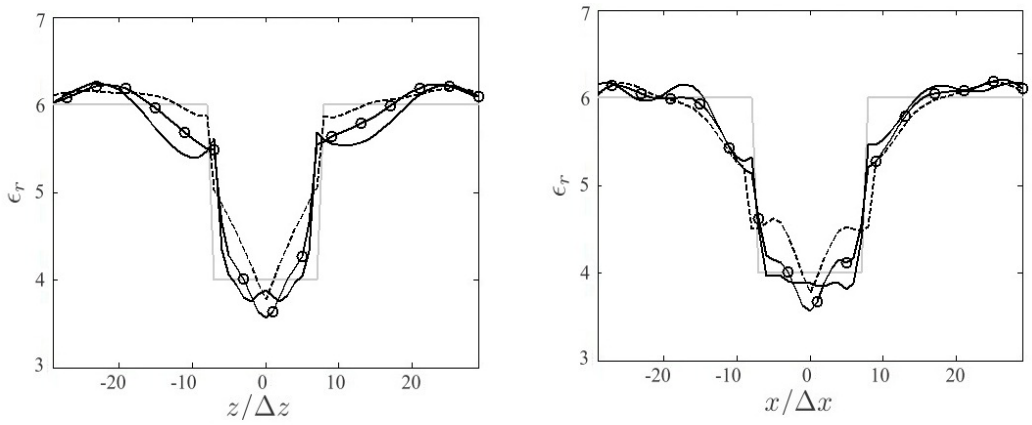

Figure 6. Recovered permittivity profile of the rectangular target described in Fig. 3, (a) at $x = 0$, (b) at $z = 0$; ——— (grey): original, − − −: stage 2 with D' bound by $\epsilon_r \leq 5$, — ∘ — : stage 3 with $\alpha = 2$, ———: stage 3 with $\alpha = 4$.

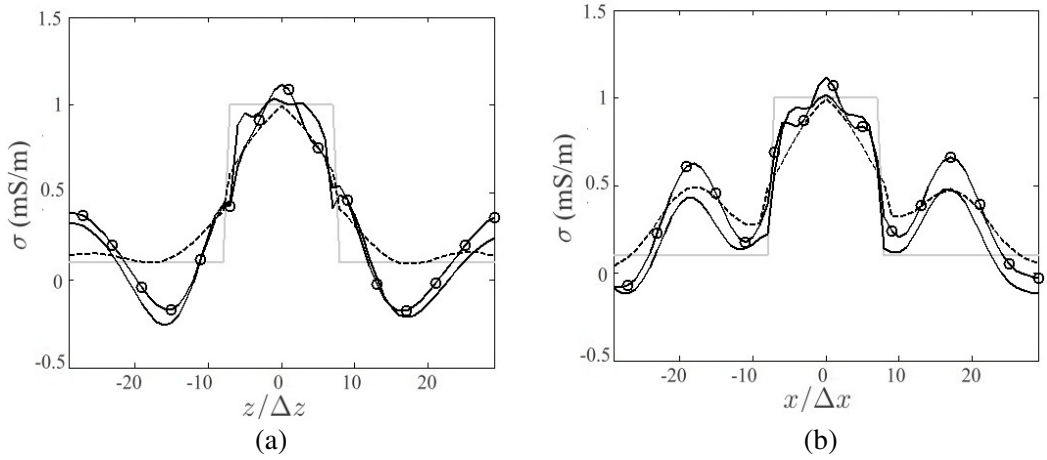

Figure 7. Recovered conductivity profile of the rectangular target described in Fig. 3, (a) at $x = 0$, (b) at $z = 0$; curve legends are the same as in Fig. 6.

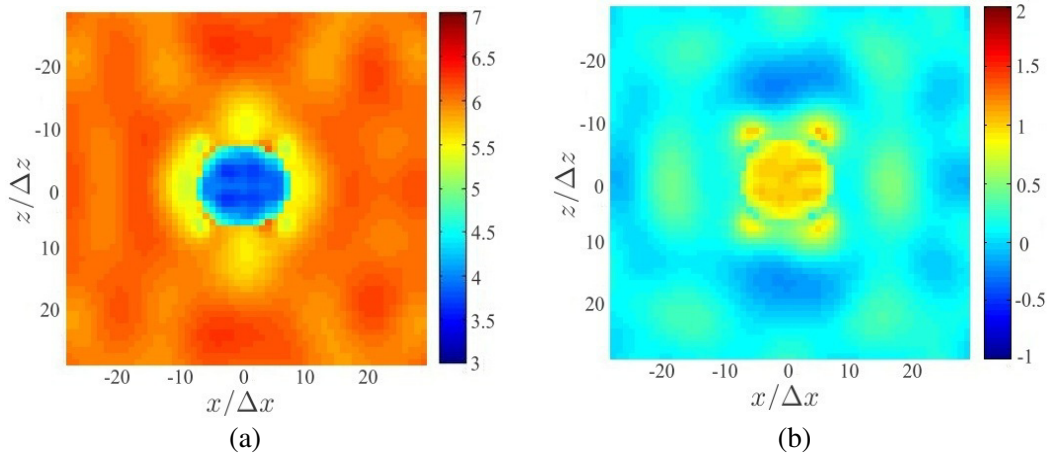

Figure 8. Recovered distributions, in stage 3 with $\alpha = 4$, of (a) relative permittivity and (b) conductivity, of the rectangular target described in Fig. 3.

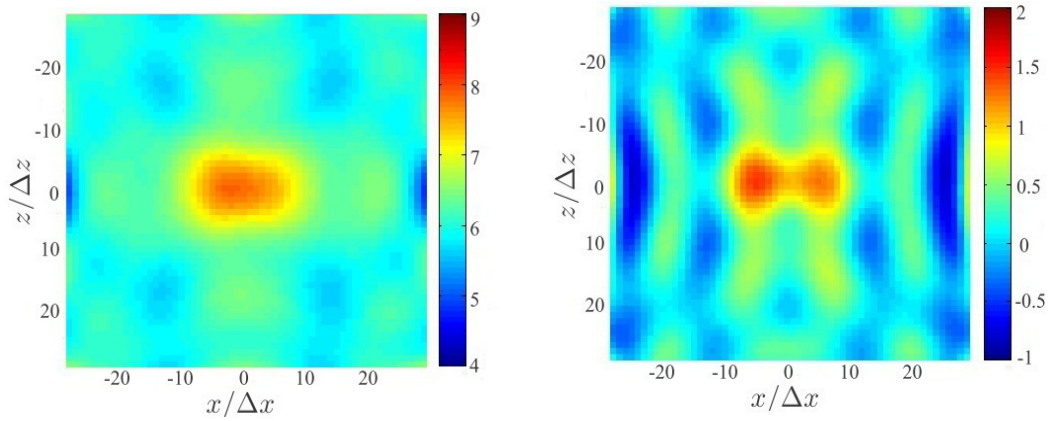

Figure 9. Recovered distributions of (a) relative permittivity and (b) conductivity, after stage 1, with a rectangular target of $\epsilon_r = 8$ and $\sigma = 1\,\mathrm{mS/m}$ embedded in a background of $\epsilon_r = 6$ and $\sigma = 0.1\,\mathrm{mS/m}$.

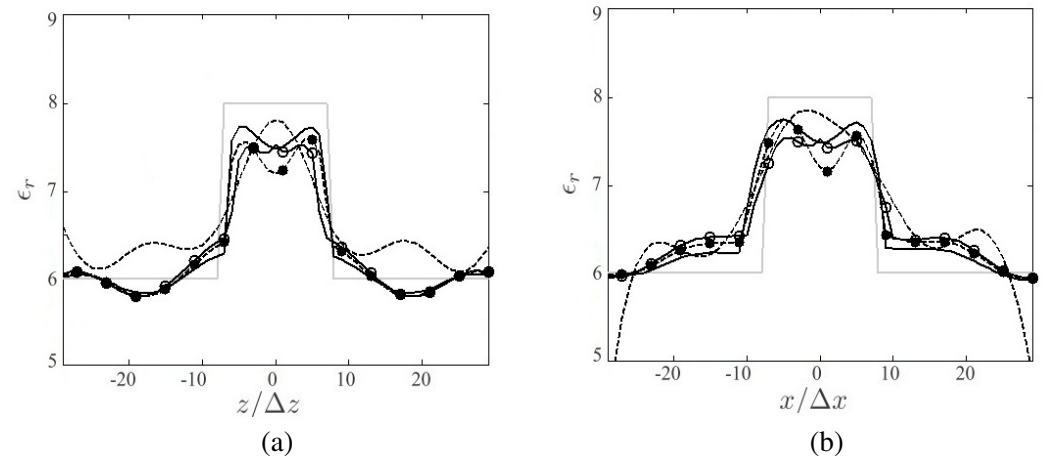

Figure 10. Recovered permittivity profile of the rectangular target described in Fig. 9, (a) at $x = 0$, (b) at $z = 0$; ——— (grey): original, − − −: stage 1, — ∘ — : stage 2 with D' bound by $\epsilon_r \leq 7.1$, − − • − − : stage 3 with $\alpha = 2$, ———: stage 3 with $\alpha = 4$.

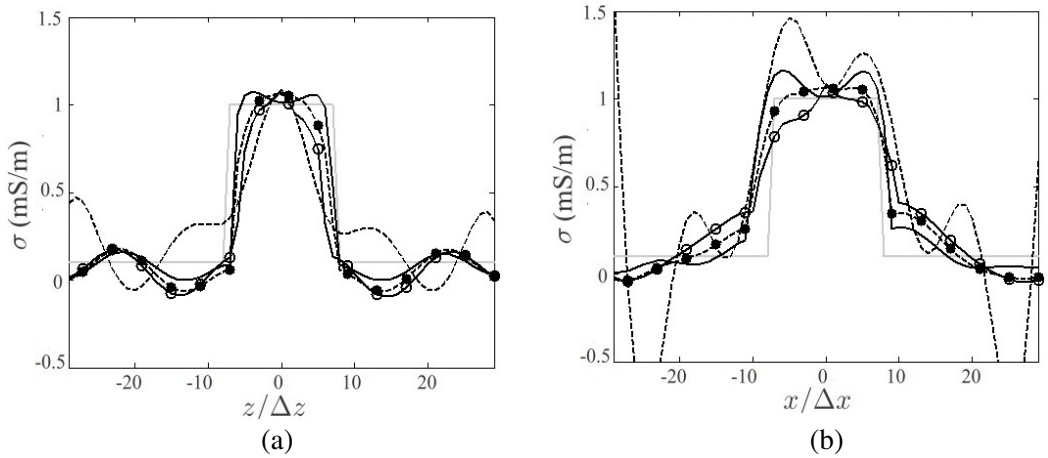

Figure 11. Recovered conductivity profile of the rectangular target described in Fig. 9, (a) at $x = 0$, (b) at $z = 0$; curve legends are the same as in Fig. 10.

with $\alpha = 1$. The target boundary becomes clearer as compared to stage 1, and the conductivity profile becomes more accurate.

In stage 3, the background distributions of ϵ and σ within D' are updated using (10) and (11), with $\alpha = 2$ or 4. Fig. 12 shows the recovered distributions with $\alpha = 4$. Compared with Fig. 9, the conductivity profile becomes more accurate, the target boundary becomes clearer than that in stage 1, the distributions within the target become more uniform, and the ripples outside the target are reduced.

In summary, the target boundary becomes clearer after stage 2 and stage 3. The distributions within the target domain, after stage 3 with $\alpha = 4$, become more uniform than those after stage 2. The recursive approach apparently improves the image quality using the conventional LSM and CSI method.

In a practical well-logging environment for exploring oil shale, a horizontally elongated target is of interest. Thus, we consider a rectangular target of width $w = 10\,\text{m}$, height $h = 3\,\text{m}$, $\epsilon_r = 4$ and $\sigma = 1\,\text{mS/m}$, embedded in limestone with $\epsilon_r = 6$ and $\sigma = 0.1\,\text{mS/m}$. Fig. 13 shows the recovered distributions of permittivity and conductivity, respectively, after stage 1. The equi-ϵ_r contours within the target domain is not as obvious as in the previous two examples, but the equi-ϵ_r around the target boundary are still roughly conformal to the original target shape. Random ripples are also observed in the distribution of ϵ_r outside the target domain, as in the previous examples.

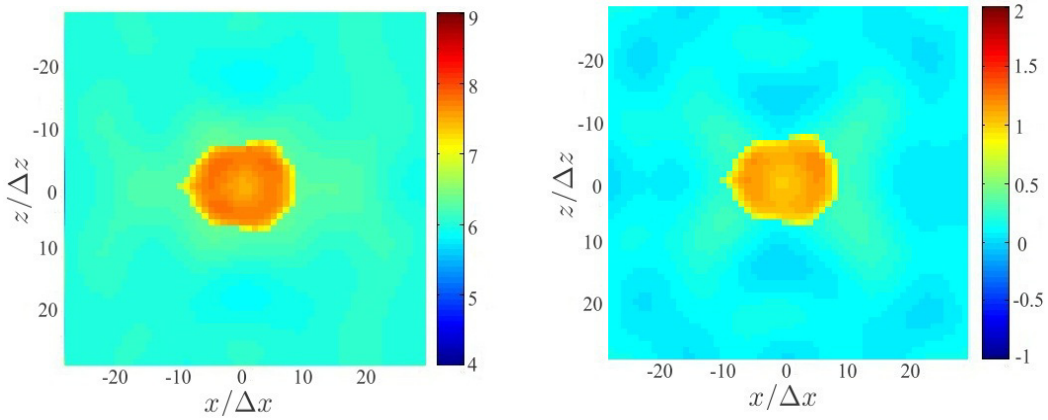

Figure 12. Recovered distributions, in stage 3 with $\alpha = 4$, of (a) relative permittivity and (b) conductivity, of the rectangular target described in Fig. 9.

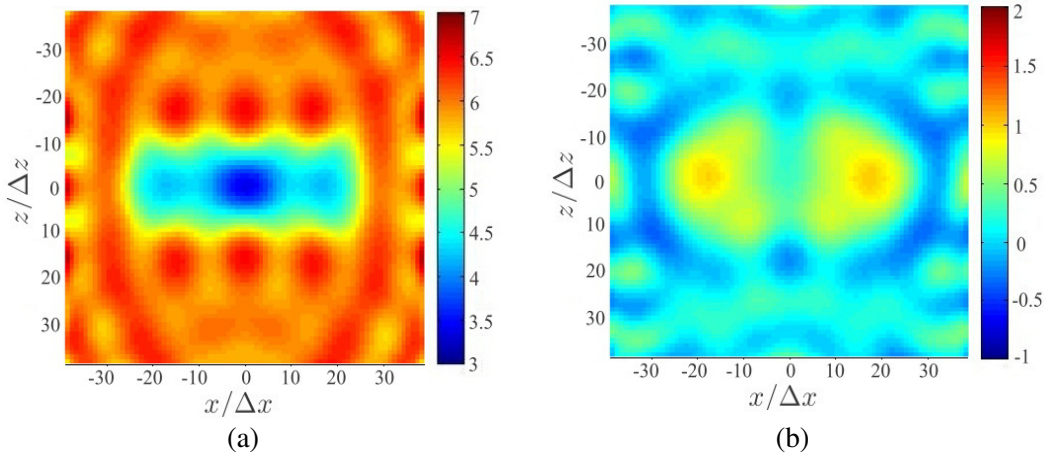

Figure 13. Recovered distributions of (a) relative permittivity and (b) conductivity, after stage 1, with an elongated rectangular target of width $w = 10\,\text{m}$, height $h = 3\,\text{m}$, $\epsilon_r = 4$ and $\sigma = 1\,\text{mS/m}$, embedded in a background of $\epsilon_r = 6$ and $\sigma = 0.1\,\text{mS/m}$.

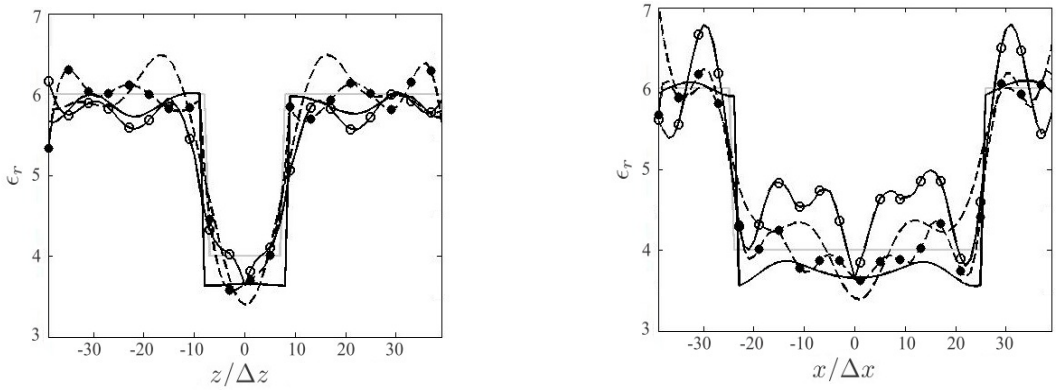

Figure 14. Recovered permittivity profile of the elongated rectangular target described in Fig. 13, (a) at $x = 0$, (b) at $z = 0$; ——— (grey): original, $- - -$: stage 1, — ∘ — : stage 2 with D' bound by $\epsilon_r \leq 5.5$, $- - \bullet - -$: stage 3 using (10) and (11) with $\alpha = 4$, ———: stage 3 using (12) and (13) with $\alpha_1 = 4$ and $\alpha_2 = 2$.

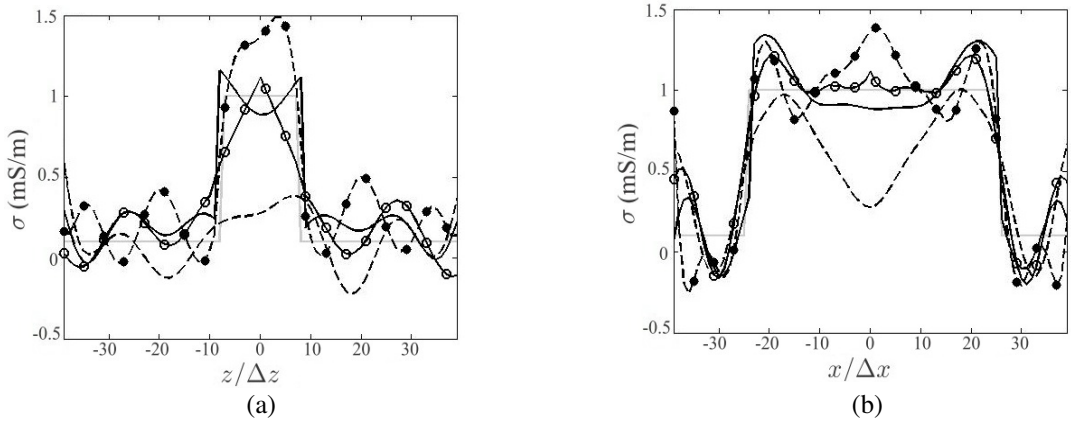

Figure 15. Recovered conductivity profile of the elongated rectangular target described in Fig. 13, (a) at $x = 0$, (b) at $z = 0$; curve legends are the same as in Fig. 14.

Figures 14 and 15 show the recovered permittivity and conductivity profiles, respectively, after stage 2 and stage 3. In stage 2, the contour of $\epsilon_r = 5.5$, based on the results in stage 1, is adopted as the target domain, D'. The background distributions of ϵ_r and σ within D' are updated using (10) and (11), respectively. The target boundary becomes clearer than that after stage 1, but not as clear as in the previous two examples. The distribution of σ within D' becomes more accurate, but the distribution of ϵ_r within D' does not improve to the same extent.

In stage 3, the background distributions of ϵ_r and σ within D' are updated using (10) and (11), with $\alpha = 4$. The target boundary turns out to be similar to that after stage 2, but the distribution of ϵ_r within the target domain becomes closer to the original one.

For an elongated target, (10) and (11) are adapted to be

$$\epsilon_b'(\bar{r}) = \epsilon_{er} + (\epsilon_b - \epsilon_{er}) \left(\frac{|x - x_c|}{|x_e - x_c|} \right)^{\alpha_1} \left(\frac{|z - z_c|}{|z_e - z_c|} \right)^{\alpha_2} \tag{12}$$

$$\sigma_b'(\bar{r}) = \sigma_{er} + (\sigma_b - \sigma_{er}) \left(\frac{|x - x_c|}{|x_e - x_c|} \right)^{\alpha_1} \left(\frac{|z - z_c|}{|z_e - z_c|} \right)^{\alpha_2} \tag{13}$$

By choosing $\alpha_1 = 4$ and $\alpha_2 = 2$, the distribution of ϵ_r within D' is further improved over that using (10) and (11).

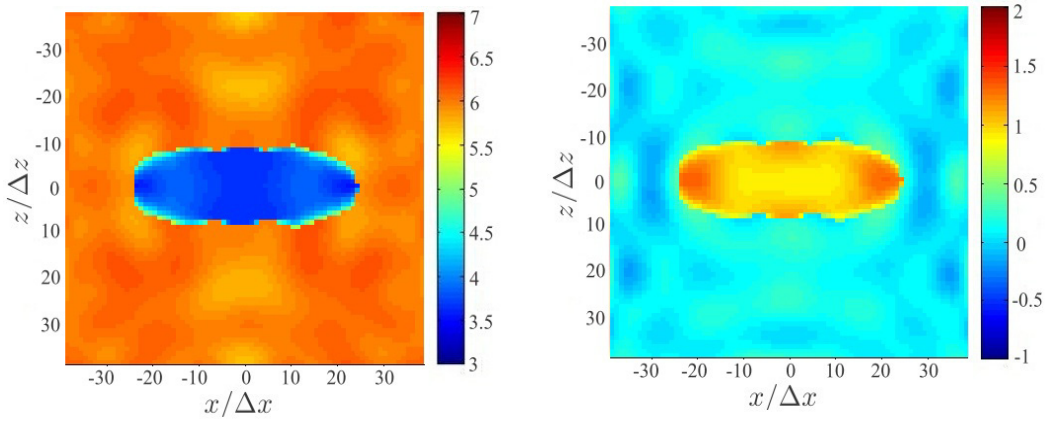

Figure 16. Recovered distributions, in stage 3 with $\alpha_1 = 4$ and $\alpha_2 = 2$, of (a) relative permittivity and (b) conductivity; of the elongated rectangular target described in Fig. 13.

Figure 16 shows the recovered distributions after stage 3, using (12) and (13). Compared with Fig. 13, the conductivity distribution becomes more accurate, and the target boundary becomes sharper than that after stage 1.

Next, we analyze the effect of noises on the recovered distributions by assuming Gaussian random noises with variance δ^2, which is related to the mean squared magnitude of the electric field at all the receiving probes, $\langle |E_t|^2 \rangle$, as $\delta^2 = \langle |E_t|^2 \rangle 10^{-\mathrm{SNR}/10}$, where SNR stands for signal-to-noise ratio. Five different percentage errors are defined as

$$\varepsilon_s = 100 \times \frac{\text{area of mismatch}}{\text{total target area}}\% \tag{14}$$

$$\varepsilon_{\epsilon t} = 100 \times \sqrt{\frac{\sum_{n=1}^{N_t} \left|\epsilon_{t,n}^e - \epsilon_{t,n}^r\right|^2}{\sum_{n=1}^{N_t} \left|\epsilon_{t,n}^r\right|^2}}\%, \qquad \varepsilon_{\sigma t} = 100 \times \sqrt{\frac{\sum_{n=1}^{N_t} \left|\sigma_{t,n}^e - \sigma_{t,n}^r\right|^2}{\sum_{n=1}^{N_t} \left|\sigma_{t,n}^r\right|^2}}\% \tag{15}$$

$$\varepsilon_{\epsilon b} = 100 \times \sqrt{\frac{\sum_{n=1}^{N_b} \left|\epsilon_{b,n}^e - \epsilon_{b,n}^r\right|^2}{\sum_{n=1}^{N_b} \left|\epsilon_{b,n}^r\right|^2}}\%, \qquad \varepsilon_{\sigma b} = 100 \times \sqrt{\frac{\sum_{n=1}^{N_b} \left|\sigma_{b,n}^e - \sigma_{b,n}^r\right|^2}{\sum_{n=1}^{N_b} \left|\sigma_{b,n}^r\right|^2}}\% \tag{16}$$

where ε_s is the shape error, $\varepsilon_{\epsilon t}$ and $\varepsilon_{\epsilon b}$ are the error of permittivity in the target area and the background, respectively; $\varepsilon_{\sigma t}$ and $\varepsilon_{\sigma b}$ are the error of conductivity in the target area and the background, respectively; N_t and N_b are the number of cells in the target area and the background, respectively; mismatch in the shape error means either a target pixel is categorized as a background pixel or vice versa; superscripts e and r stand for the estimated value and the real value, respectively; and subscript t and b stand for the target area and the background, respectively.

Figure 17 shows the effect of noise on the recovered distributions related to that in Fig. 16.

Finally, consider a target size closer to that in practical well-logging environment for exploring oil shale: An elongated rectangular target of width $w = 200\,\mathrm{m}$, height $h = 60\,\mathrm{m}$, $\epsilon_r = 4$ and $\sigma = 0.1\,\mathrm{mS/m}$, mimicking a high-yield oil shale [15], is embedded in limestone with $\epsilon_r = 6$ and $\sigma = 0.01\,\mathrm{mS/m}$ [16, 17]. The operating frequency is 1 MHz. The two boreholes are separated by $s = 400\,\mathrm{m}$, with 21 probes in each borehole, at a spacing of $d = 20\,\mathrm{m}$. The cell size is $\Delta x = \Delta z = 4\,\mathrm{m}$.

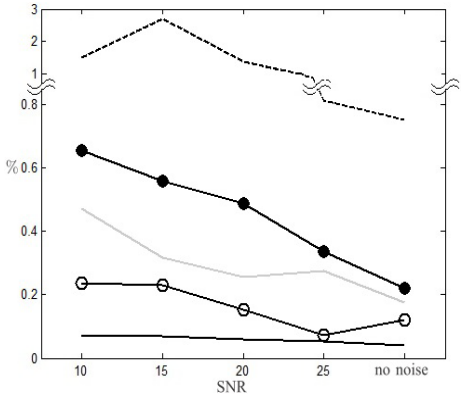

Figure 17. Effect of noise on the percentage errors related to the distributions in Fig. 16. ——— (grey): ε_s, − − −: $\varepsilon_{\epsilon t}$, − ∘ −: $\varepsilon_{\epsilon b}$, ———: $\varepsilon_{\sigma t}$, − • −: $\varepsilon_{\sigma b}$.

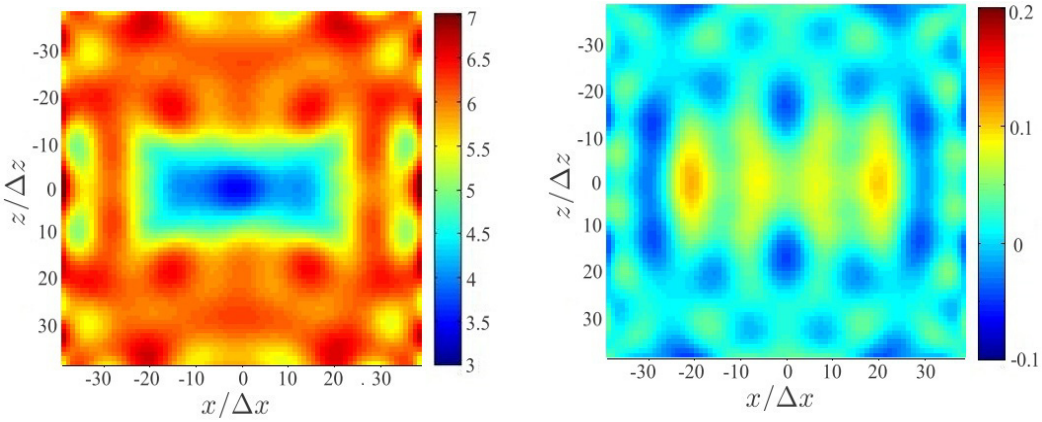

Figure 18. Recovered distributions, after stage 1, of (a) relative permittivity and (b) conductivity. A field-size rectangular target of width $w = 200\,\text{m}$, height $h = 60\,\text{m}$, $\epsilon_r = 4$ and $\sigma = 0.1\,\text{mS/m}$, is embedded in a background of $\epsilon_r = 6$ and $\sigma = 0.01\,\text{mS/m}$.

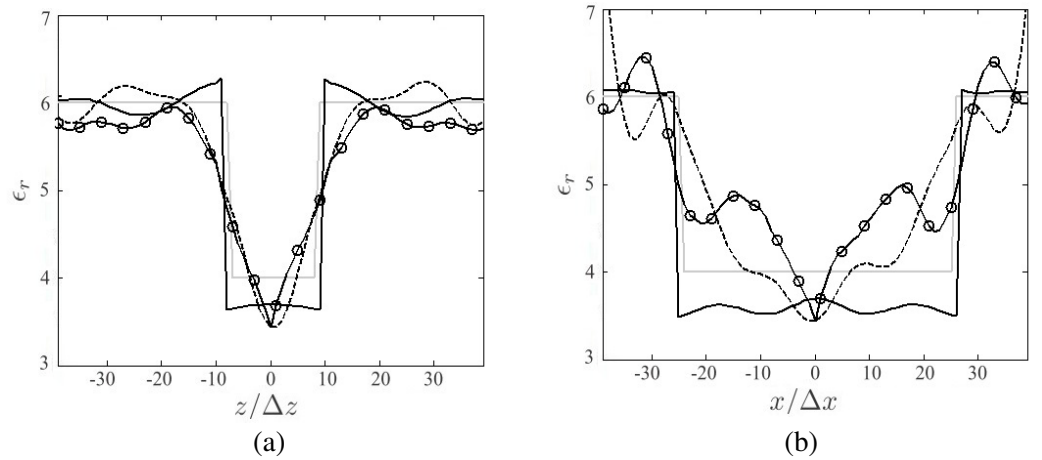

Figure 19. Recovered permittivity profile of the rectangular target described in Fig. 18, (a) at $x = 0$, (b) at $z = 0$; ——— (grey): original, − − −: stage 1, — ∘ —: stage 2 with D' bound by $\epsilon_r \leq 5.4$, ———: stage 3 using (12) and (13), with $\alpha_1 = 4$ and $\alpha_2 = 2$.

Figure 18 shows the recovered distributions of permittivity and conductivity after stage 1. The equi-ϵ_r contours within the target domain are not as obvious as in Fig. 13 (at 20 MHz), and more random ripples appear in the distribution of ϵ_r outside the target domain.

Figures 19 and 20 show the recovered permittivity and conductivity profiles, respectively, after stage 3. In stage 2, the contour of $\epsilon_r = 5.4$, based on the results in stage 1, is chosen as the target domain, D'. The background distributions of ϵ_r and σ within D' are updated using (10) and (11). The target boundary becomes sharper than that after stage 1, but not as clear as in the previous examples probed at 20 MHz. The distribution of σ within D' becomes more accurate, but the distribution of ϵ_r within D' does not improve as much as in the previous examples probed at 20 MHz.

In stage 3, the background distributions of ϵ_r and σ within D' are updated using (12) and (13), with $\alpha_1 = 4$ and $\alpha_2 = 2$. The target boundary becomes closer to the original one, but the value of ϵ_r within the target is slightly under-estimated.

Figure 21 shows the recovered distributions after stage 3, using (12) and (13). Compared with Fig. 18, the conductivity profile becomes more accurate, and the target boundary appears sharper than that after stage 1.

Figure 22 shows the effect of noise on the distribution related to that in Fig. 21.

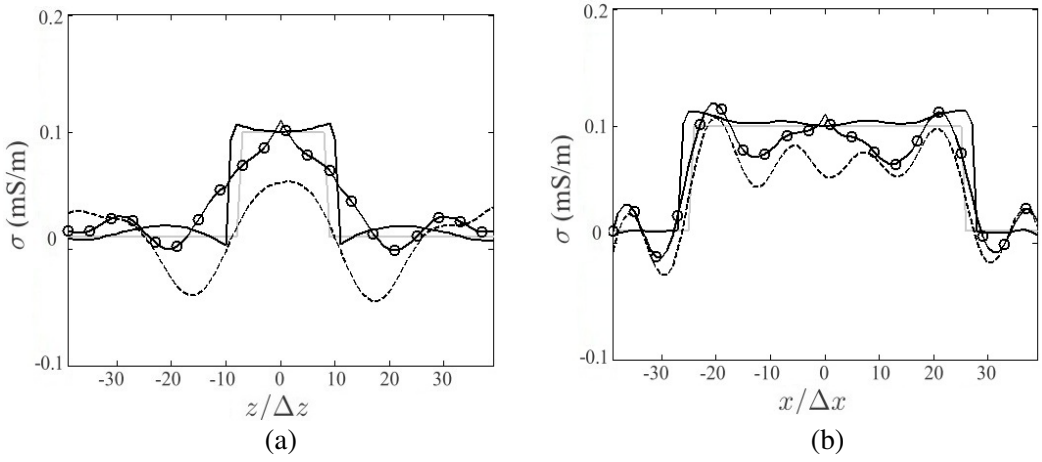

Figure 20. Recovered conductivity profile of the rectangular target described in Fig. 18, (a) at $x = 0$, (b) at $z = 0$; curve legends are the same as in Fig. 19.

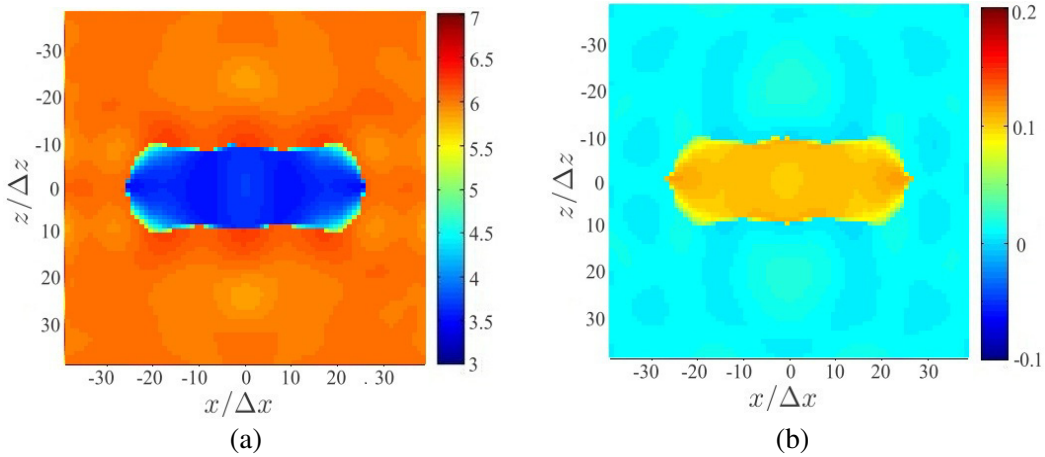

Figure 21. Recovered distributions, in stage 3 with $\alpha_1 = 4$ and $\alpha_2 = 2$, of (a) relative permittivity and (b) conductivity; of the rectangular target described in Fig. 18.

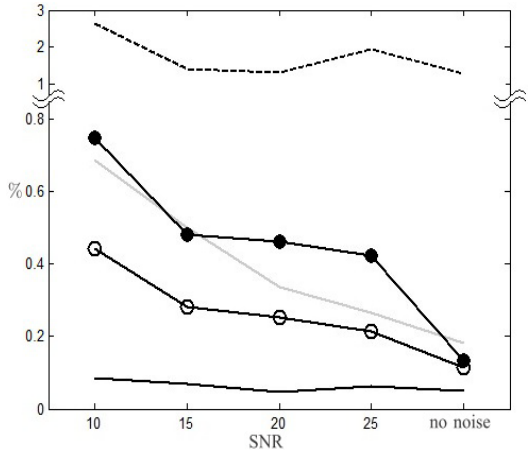

Figure 22. Effect of noise on the percentage errors related to the distributions in Fig. 21. ——— (grey): ε_s, − − −: $\varepsilon_{\epsilon t}$, − ○ −: $\varepsilon_{\epsilon b}$, ———: $\varepsilon_{\sigma t}$, − ● −: $\varepsilon_{\sigma b}$.

4. CONCLUSION

A three-stage recursive approach, using the conventional linear sampling method (LSM) and the contrast source inversion (CSI) method in the first stage, is proposed to enhance the contrast between the targets and the background. The second stage is proposed to acquire a sharper target shape, and the third stage is proposed to improve the distributions of permittivity and conductivity more accurately. By simulations, this recursive approach proves to improve the contrast between the target and the background, and the random ripples are significantly reduced.

ACKNOWLEDGMENT

This work was sponsored by the National Science Council, Taiwan, under contract NSC 101-2221-E-002-129; and the Ministry of Education, Taiwan, under Aim for Top University Project 103R3401-1.

REFERENCES

1. Crocco, L., I. Catapano, L. D. Donato, and T. Isernia, "The linear sampling method as a way to quantitative inverse scattering," *IEEE Trans. Antennas Propagat.*, Vol. 60, No. 4, 1844–1853, Apr. 2012.
2. Catapano, I., L. Crocco, and T. Isernia, "Improved sampling methods for shape reconstruction of 3-D buried targets," *IEEE Trans. Geosci. Remote Sens.*, Vol. 46, No. 10, 3265–3273, Oct. 2008.
3. Constable, S. C., R. L. Parker, and C. G. Constable, "The linear sampling method in inverse electromagnetic scattering theory," *Inverse Problems*, Vol. 19, No. 6, S105–137, 2003.
4. Gilmore, C., A. Abubakar, W. Hu, T. M. Habashy, and P. M. van den Berg, "Microwave biomedical data inversion using the finite-difference contrast source inversion method," *IEEE Trans. Antennas Propagat.*, Vol. 57, No. 5, 1528–1538, May 2009.
5. Abubakar, A., W. Hu, P. M. van den Berg, and T. M. Habashy, "A finite-difference contrast source inversion method," *Inverse Problems*, Vol. 24, 065004, 2008.
6. Van den Berg, P. M. and R. E. Kleinman, "A contrast source inversion method," *Inverse Problems*, Vol. 13, No. 6, 1607–1620, 1997.
7. Abubaker, A., P. M. van den Berh, and J. J. Mallorqui, "Imaging of biomedical data using a multiplicative regularized contrast source inversion method," *IEEE Trans. Microwave Theory Tech.*, Vol. 50, No. 7, 1761–1771, Jul. 2002.

8. Gilmore, C., P. Mojabi, and J. LoVetri, "Comparison of an enhanced distorted Born iterative method and the multiplicative-regularized contrast source inversion method," *IEEE Trans. Antennas Propagat.*, Vol. 57, No. 8, 2341–2350, Aug. 2009.
9. Binley, A. and A. Kemna, "DC resistivity and induced polarization methods," *Hydrogeophy.*, Vol. 50, 129–156, 2005.
10. Ernst, J. R., H. Maurer, A. G. Green, and K. Holloger, "Full-waveform inversion of crosshole radar data based on 2-D finite-difference time-domain solution of Maxwell's equations," *IEEE Trans. Geosci. Remote Sens.*, Vol. 45, No. 9, 2807–2826, Sep. 2007.
11. Pralat, A. and R. Zdunek, "Electromagnetic geotomography-selection of measuring frequency," *IEEE Sens. J.*, Vol. 5, No. 2, 242–250, Apr. 2005.
12. Spies, B. R., "Electrical and electromagnetic borehole measurement: A review," *Survey Geophys.*, Vol. 17, 517–556, 1996.
13. Zhou, H., M. Sato, T. Takenaka, and G. Li, "Reconstruction from antenna-transformed radar data using a time-domain reconstruction method," *IEEE Trans. Geosci. Remote Sens.*, Vol. 45, No. 9, 689–696, Mar. 2007.
14. Meles, G. A., J. V. der Kruk, S. A. Greenhalgh, J. R. Ernst, H. Murer, and A. G. Green, "A new vector waveform inversion algorithm for simultaneous updating of conductivity and permittivity parameters from combination crosshole/borehole-to-surface GPR data," *IEEE Trans. Geosci. Remote Sens.*, Vol. 48, No. 9, 3391–3407, Sep. 2010.
15. Jesch, R. L. and R. H. McLaughlin, "Dielectric measurements of oil shale as functions of temperature and frequency," *IEEE Trans. Geosci. Remote Sens.*, Vol. 39, No. 12, 2713–2721, Dec. 2001.
16. Schon, J. H., *Physical Properties of Rocks*, Elsevier, 2011.
17. Dyni, J. R., "Geology and resources of some world oil-shale deposits," U.S. Geolog. Survey Sci. Investig. Rep., 2006.